

This figure "m15_fig1.jpg" is available in "jpg" format from:

<http://arxiv.org/ps/astro-ph/9701030v1>

TABLE 1. Star Counts

Radius (arcsec)	Number of stars per square arcsecond		
	$18.25 < V < 19.75$	$19.75 < V < 21.25$	$21.25 < V < 22.75$
0.31	32.0 ± 8.6
0.71	32.4 ± 9.3
0.89	18.5 ± 4.6
1.12	14.7 ± 2.9	52.5 ± 7.1	...
1.41	19.5 ± 3.2	43.6 ± 5.6	...
1.78	13.6 ± 2.1	33.8 ± 3.6	...
2.24	10.4 ± 1.3	30.8 ± 2.5	...
2.82	9.8 ± 1.1	18.9 ± 1.5	...
3.55	7.5 ± 0.8	23.0 ± 1.5	24.6 ± 2.0
4.47	7.2 ± 0.8	18.8 ± 1.3	24.4 ± 1.9
5.62	5.5 ± 0.8	16.5 ± 1.4	19.0 ± 1.7
7.08	5.4 ± 0.8	12.6 ± 1.3	13.0 ± 1.5
8.91	2.8 ± 1.1	10.6 ± 2.1	10.4 ± 2.3

This figure "m15_fig2.jpg" is available in "jpg" format from:

<http://arxiv.org/ps/astro-ph/9701030v1>

TABLE 2. Mass Functions

Mass (M_{\odot})	(# stars) / (square arcsec) (unit mass)	
	$3'' < r < 8''$	$r = 20''$
0.78	174.5 ± 19.2	...
0.77	222.6 ± 16.9	...
0.75	208.9 ± 13.7	35.1 ± 5.3
0.72	172.5 ± 10.9	38.3 ± 4.9
0.68	174.7 ± 10.2	43.3 ± 4.8
0.64	144.7 ± 9.2	46.2 ± 4.9
0.60	160.3 ± 9.6	46.4 ± 4.9
0.56	...	46.6 ± 4.9
0.52	...	47.2 ± 4.7
0.47	...	41.8 ± 4.0

This figure "m15_fig3.jpg" is available in "jpg" format from:

<http://arxiv.org/ps/astro-ph/9701030v1>

TABLE 3A. King-model parameters

r_c	0.01 pc = 0''2
r_t	60.0 pc = 20'
r_a	22.0 pc = 7'3
W_0	30.2
Total cluster mass	$3.42 \times 10^5 M_\odot$
Total number of stars	9.49×10^5
ρ_0	$2.81 \times 10^7 M_\odot/\text{pc}^3$

Notes to Table 3a.

Entries in this table refer to cluster model parameters as defined by Gunn & Griffin (1979).

TABLE 3B. King-model mass function

Mass (M_\odot)	Total mass fraction	Central density fraction
0.787	0.0578	1.189×10^{-2}
0.743	0.0564	6.598×10^{-3}
0.690	0.0492	2.871×10^{-3}
0.634	0.0566	1.556×10^{-3}
0.577	0.0625	7.943×10^{-4}
0.521	0.0740	4.404×10^{-4}
0.455	0.0721	1.777×10^{-4}
0.378	0.0661	6.060×10^{-5}
0.290	0.0818	2.634×10^{-5}
0.226	0.0735	1.197×10^{-5}
0.181	0.0490	5.188×10^{-6}
0.149	0.0426	3.399×10^{-6}
0.124	0.0414	2.717×10^{-6}
0.550	0.2093	1.845×10^{-3}
1.500	0.0078	9.738×10^{-1}

This figure "m15_fig4.jpg" is available in "jpg" format from:

<http://arxiv.org/ps/astro-ph/9701030v1>

To appear in the *Astronomical Journal*, April 1997

Deep *HST*/FOC Imaging of the Central Density Cusp of the Globular Cluster M15¹

Craig Sosin and Ivan R. King

Astronomy Department, University of California, Berkeley, CA 94720

Electronic mail: csosin@astro.berkeley.edu, king@astro.berkeley.edu

ABSTRACT

Using the Faint Object Camera on the repaired *Hubble Space Telescope*, we have observed two fields in the globular cluster M15: the central density cusp, and a field at $r = 20''$. These are the highest-resolution images ever taken of this cluster's dense core, and are the first to probe the distribution of stars well below the main-sequence turnoff. After correction for incompleteness, we measure a logarithmic cusp slope ($d \log \sigma / d \log r$) of -0.70 ± 0.05 (1-sigma) for turnoff ($\sim 0.8M_{\odot}$) stars over the radial range from $0''.3$ to $10''$; this slope is consistent with previous measurements. We also set an approximate upper limit of $\sim 1''.5$ (90% confidence limit) on the size of any possible constant-surface-density core, but discuss uncertainties in this limit that arise from crowding corrections. We find that fainter stars in the cusp also have power-law density profiles: a mass group near $0.7M_{\odot}$ has a logarithmic slope of -0.56 ± 0.05 (1-sigma) over the radial range from $2''$ to $10''$. Taken together, the two slopes are not well matched by the simplest core-collapse or black-hole models. We also measure a mass function at $r = 20''$, outside of the central cusp. Both of the FOC fields show substantial mass segregation, when compared with a mass function measured with the WFPC2 at $r = 5'$. In comparing the overall mass functions of the two FOC fields and the $r = 5'$ field, we find that the radial variation of the mass function is somewhat less than that predicted by a King–Michie model of the cluster, but greater than that predicted by a Fokker–Planck model taken from the literature.

Subject headings: globular clusters—stellar systems (kinematics, dynamics)

¹Based on observations with the NASA/ESA *Hubble Space Telescope*, obtained at the Space Telescope Science Institute, which is operated by AURA, Inc., under NASA contract NAS 5-26555.

1. Introduction

For years, studies of M15 have guided our understanding of the dynamical evolution of globular clusters. Observations have shown that the cluster’s stellar density rises in its center in a power-law cusp, with no sign of a “flat,” constant-surface-density core at the resolution attainable from the ground (Djorgovski & King 1984, Lugger *et al.* 1987). Most researchers have considered M15 to be in a state of core collapse, in which the cluster core’s negative heat capacity has resulted in its runaway contraction. The collapse would eventually be halted by energy input from binary stars (see the references in Hut & Makino 1996). Alternatively, M15 could harbor a massive ($\sim 10^3 M_\odot$) black hole in its center; the cusp would then be a result of the black hole’s deep potential well (Bahcall & Wolf 1976).

The increase in resolving power provided by the *Hubble Space Telescope* (*HST*) can help to determine the nature of the density cusp. The principal goal of *HST* observations of M15 has been to resolve stars near the main-sequence turnoff, since the large number of such stars should trace the stellar density profile much more clearly than the handful of bright giants seen from the ground.

Early *HST* results, though, provided more confusion than clarity: until the 1993 repair, most of the light of the bright stars was spread into an extended “halo” that obscured the view of the faint stars. Lauer *et al.* (1991) attempted to subtract these bright stars from a *U*-band Planetary Camera image of the M15 cusp, and claimed the detection of a “flat” (constant surface-density) core of radius $2''.2$ in the residual light. Yanny *et al.* (1994), however, found a serious flaw in this procedure: stellar-photometry software attributes too much of the light to the bright stars in a crowded field, at the expense of their faint neighbors. The bright stars are thus oversubtracted in the densest region near the cluster center, creating the illusion of a flat core.

Guhathakurta *et al.* (1996, hereafter GYSB) followed up the Yanny *et al.* study by taking post-repair WFPC2 images of the M15 cusp, and found that the stellar density rises all the way into $r \simeq 0''.3$. Moreover, GYSB found that the cusp surface density is well fit by a power law of slope -0.82 ± 0.12 —quite close to the slope of -0.75 expected for stars near a massive black hole, but also consistent with the outcome of core collapse in the presence of dark objects of mass $\geq 1M_\odot$ (Cohn 1985, Grabhorn *et al.* 1992).

Our main goal in this paper is to present an analysis of a set of images of the M15 cusp, taken with the Faint Object Camera (FOC) aboard the repaired *HST*. The FOC samples the *HST* point-spread function (PSF) much better than the WFPC2: its pixel scale is $0''.014/\text{pixel}$, compared to the Planetary Camera chip’s $0''.044/\text{pixel}$ (the FWHM of the *V*-band PSF is $0''.04$). In the central $2''$ of M15, the typical separation of stars with $19 < V < 21$ is $\sim 0''.15$, so the FOC can separate many more close stellar pairs.

We begin by describing the images themselves. We then describe our procedure for extracting as much photometric information as possible from the images, and the extensive

artificial-star experiments that accompany this procedure. We then use these data to construct the surface-density profiles and mass functions of M15. Finally, we construct a simple dynamical model of M15, and compare our results with a Fokker–Planck model from the literature.

2. Observations

M15 was observed by *HST* on 27 September 1994, with the COSTAR optical correction system in place. (For details of the design and performance of the camera and correction system, see Greenfield *et al.* 1991 and Jędrzejewski *et al.* 1994.) Three $\sim 7 \times 7$ -arcsecond FOC images were taken through each of the F430W (FOC “*B*”) and F480LP (FOC “*V*”) filters; the exposure times ranged from 2020.75 to 2519.75 seconds. All of the images were geometrically corrected and flatfielded by the STScI Routine Science Data Processing (RSDP) pipeline.

The inner two FOC fields overlap slightly, and together cover a $\sim 13 \times 7$ -arcsec region around the cluster center. Their combined *V* images are shown in Figure 1. We reduced these images in their original form, but then immediately transformed the results to a common coordinate system; the combined field will be called the “central field” in what follows. In this study, we analyzed only the *V* images of the central field, since the *B* images suffer badly from detector saturation.

The third *B* and *V* pair of images were taken of a field 20 arcseconds out from the cluster center; the *V* image is shown in Figure 2. This field is devoid of bright stars, so that both the *B* and *V* images are suitable for analysis. The lesser degree of stellar crowding and the lower background of scattered light allow the photometry of the $r = 20''$ field to go to $V = 24$, one or two magnitudes deeper than in the central field.

A closeup of the central $\sim 3.5 \times 3.5$ arcseconds of M15 is shown in Figure 3, with stars of various *V* magnitudes indicated. Note that the large crescent-shaped “objects” are bright, saturated stars; their shape is a result of peculiarities of the FOC photon-event detection logic. The FOC saturates at high count *rate*, rather than at high *numbers* of counts, so the saturation cannot be removed by taking an additional set of short exposures. (FOC images can be taken through neutral-density filters, if information about bright stars is needed. In the case of M15, short exposures of the center have already been taken with the WFPC2, by GYSB.)

Looking at Fig. 3, one’s immediate impression is that the stellar density continues to rise into the very center of the cluster, and does not level off at $r \simeq 2''$, as suggested by pre-repair work (Lauer *et al.* 1991). To some degree, this impression is a result of the higher background level created by scattered light from a few bright stars, whose chance placements near the center do not imply a significantly higher stellar density. One goal of our analysis will be to use the larger number of turnoff-magnitude stars to determine whether a $2''$ core is present.

3. Photometry

In this section and the next, we describe our procedure for image reduction and analysis. We begin, in §3, by describing the photometry—in particular, methods for finding faint stars and rejecting false detections in crowded regions. In §4, we describe the artificial-star experiments that allow us to correct for the errors induced by crowding.

The crowding of stars in this field has led to some controversy over observational results in recent years. With this fact in mind, we devoted a great deal of attention to analysis methods, and will describe them in some detail. Readers interested only in the results of the analysis will find those results in the latter half of §5 and in §6.

3.1. The central field

First, it is apparent from Figures 1 and 2 that parts of the images ($\sim 10\%$) are unusable because of the presence of saturated ($V < 18$) stars. We identify these regions by hand before beginning, and exclude them from any further analysis.

The stellar photometry package DAOPHOT (Stetson 1987, 1992) has become a standard tool for globular-cluster image analysis, and we adopt it here. DAOPHOT was originally designed for ground-based images, in which the point-spread function (PSF) is nearly Gaussian in its center, and decreases monotonically at larger radii. *HST* is diffraction-limited, though, and the FOC has a small enough pixel size that the innermost diffraction rings are “resolved” quite clearly (see Fig. 3). When used with FOC images, the FIND algorithm in DAOPHOT often identifies several false “objects” on the first diffraction ring of each star, and thus finds “clusters” of objects four or five pixels apart.

It is important, then, to reject such false detections, while throwing away as few *real* objects as possible (since many objects do happen to fall on the diffraction ring of another star). We have developed a three-pass procedure to do so:

First pass. To begin, we use DAOPHOT FIND to identify stars, and also “find” nearly three times as many false detections. We then compare the central pixel of each detection to the highest pixel in an annulus between 4.5 and 5.5 pixels from that central pixel. False detections on diffraction rings will always have a high peak—the star’s true PSF core—in the annulus, while most true detections will not (except for those that have bright close neighbors). We exclude, for the remainder of the first pass, any detection whose highest pixel in the annulus is more than twice as high as its central pixel. (Isolated real stars, on the other hand, have a central pixel that is 5–10 times higher than the highest pixel in the annulus.)

The remaining list contains perhaps 80% of the stars that will ultimately be identified, and has *no* false detections. We then complete the standard DAOPHOT reduction sequence using this

preliminary list of objects: aperture photometry, determination of the PSF using isolated stars (selected manually), and PSF-fitting, to obtain a preliminary magnitude for each star. (The PSF determination was actually iterated two or three times, with neighbors of the PSF stars subtracted on the later iterations.)

Figure 4a shows a small section of the original image of our central field. Figure 4b shows the same section after stars have been subtracted using the first-pass magnitudes. Note that a number of faint stars have been missed, at this point. The circle in Fig. 4a indicates a star with another star “hidden” in its diffraction ring; this “hidden” star is mistaken for a diffraction-ring feature by the first pass.

Second pass. We then use the results of the first pass to subtract a scaled copy of the PSF from each star in the preliminary list from the previous pass—but we subtract only those pixels that lie ≥ 4 pixels away from the central pixel of the PSF. This has the effect of removing the diffraction rings from the image (the first ring is at a radius of 5 pixels), while leaving the central peaks. Faint stars hidden *in* the diffraction rings of a brighter neighbor also remain. A section of this “ring-subtracted” image is shown in Figure 4c (note that the “hidden” star from Fig. 4a shows up clearly on Fig. 4c). We then run FIND on this ring-subtracted image, producing a second preliminary list of stellar positions.

We then use the second preliminary star list as input to the usual DAOPHOT sequence—aperture photometry and PSF-fitting—for a second time.

(Unfortunately, the brightest non-saturated stars are slightly nonlinear in their centers, so that their rings do not subtract cleanly, and false “objects” are found in the poorly-subtracted rings on the second pass. We therefore ignore all found neighbors of such stars from here on—removing a further few percent of the central field from consideration. All stars with V magnitudes brighter than 18.2 [measured in the second-pass aperture photometry step] were considered to be nonlinear; we chose this limit from a visual inspection of their appearance on the ring-subtracted image.)

Third pass. The PSF-fitting step in the second pass produces an image with all stars found thus far subtracted; see Figure 4d for an example. (The “hidden” star in Fig. 4a has now been successfully fit and subtracted.) An inspection of this image reveals a number of “double-lobed” residuals, where stars separated by $\lesssim 3$ pixels were reduced as a single star by the previous pass (one such blend is indicated by a circle in Fig. 4d).

We identify these blended close pairs on the second-pass subtracted image (Fig. 4d) as follows: At each position where a star was subtracted, our software first determines the angle ϕ along which the residual light is most elongated. Then, it measures (1) the number of residual counts F_a in a zone within 15° of this major axis, out to a radius of 5 pixels, (2) the number of counts F_b within 15° of the minor axis within the same radius, and (3) the mean distance \bar{r} of the residual flux from the stellar center.

Locations with large $F_a - F_b$ are either blended pairs mistakenly reduced as a single star,

or single objects that subtracted poorly for some other reason (most often, because they are nonlinear in their centers). The quantity \bar{r} distinguishes between these possibilities: the residual light from blends is at large radius, while that from a poorly fit single star is near the star’s center. We thus identify any subtracted “star” with $F_a - F_b > 800$ counts and $\bar{r} > 3$ pixels as a candidate blend. (A better algorithm might be to normalize the F difference by the flux of the “star,” but in practice, the 800-count criterion had the desired effect of finding the most obvious blends, without finding noise.)

We then split each candidate blend into two stars in our list, separating the two by one FWHM of the PSF, at position angle ϕ . The resulting list is run through a third and final stage of PSF-fitting, to refine the positions and magnitudes of the close pairs, and it is the output list from this step that we take as the final result of our image reduction. A portion of the final subtracted image is shown in Figure 4e. Note that some of the blends have been removed (such as the blend indicated in Fig. 4d), but not all. Artificial-star experiments will allow us to correct the star counts for the few that have been missed.

The reduction scheme may seem tedious, but it is not very “long” in terms of CPU time (a complete run, excluding the initial interactive measurement of the PSF, takes about 15 to 20 minutes on our workstation). Note that since every step is entirely automated (after the PSF measurement), artificial-star experiments require no additional human effort.

3.2. The 20'' field

We also performed stellar photometry on the B and V images of the $r = 20''$ field. The reduction scheme was the same, except that the entire third pass—the splitting of close pairs, separated by less than 3 pixels—was skipped. (Since the stars on this field are much less crowded, there are far fewer close blends, and searching for them would have been a waste of time. Our artificial-star experiments later confirmed this impression, and allowed us to correct for the few close pairs that were present.)

We then calibrated the photometry (of both the central and $r = 20''$ fields). The FOC has been calibrated by medium- and narrowband observations of spectrophotometric standards (see Greenfield *et al.* 1991). The resulting filter sensitivities are written into each image header by the RSDP pipeline; those photometric header keywords allowed our stellar magnitudes to be adjusted to the *HST* instrumental system. An *HST* magnitude m_λ is defined as $m_\lambda = -2.5 \log f_\lambda - 21.1$, where f_λ is expressed in $\text{erg cm}^{-2} \text{s}^{-1} \text{\AA}^{-1}$ at the filter’s “pivot wavelength” (4111 Å for F430W, and 5254 Å for F480LP).

We then converted our magnitudes from the *HST* instrumental system to Johnson B and V , using a transformation calculated by Jay Anderson (see King, Anderson, & Sosin 1994). The resulting color–magnitude diagram of the $r = 20''$ field is shown in Figure 5, including a small correction to be described below. Note that the FOC V_{480} magnitude is almost identical to

Johnson V , and we use V_{480} and Johnson V interchangeably in what follows.

Durrell & Harris (1993, hereafter DH93) have presented a deep ground-based CMD of a field 7' from the center of M15. Their “smoothed” fiducial main-sequence line is shown in Figure 5 (dashed line), along with the ($[\text{Fe}/\text{H}] = -2.26$, $t = 15$ Gyr) Bergbusch & Vandenberg (1992, hereafter BV92) isochrone (solid line). DH93 found this isochrone to fit the sequences in their CMD, with $(m - M)_V = 15.40$, $E(B - V) = 0.10$, and a small “color shift” of 0.015.

We needed to shift our own stellar colors redward by 0.12 mag to match the DH93 fiducial; this shift is comparable to the FOC calibration uncertainty. With this shift, our objects fit the isochrone well, so we adopt the same distance and reddening as DH93, and later will use the BV92 isochrone to convert luminosities to masses. Note that our sequence deviates to the red from the DH93 sequence at the bright end, because of the onset of detector nonlinearity in B ; the B images of these stars do in fact appear slightly distorted. The V magnitudes of the stars plotted are unaffected by nonlinearity.

Note the presence of an anomalously blue object at $V = 20.2$, $B - V = 0.3$ in Figure 5; it appears at (232, 102) on the $r = 20''$ V image, is indicated by a circle in Fig. 2, and has J2000 coordinates ($21^{\text{h}}29^{\text{m}}58^{\text{s}}.27$, $12^{\circ}10'19''.9$). Its B magnitude is strongly affected by nonlinearity, so it is probably even bluer than shown on Fig. 5. This object could be similar to the blue objects found in the core of M15 by De Marchi & Paresce (1996).

Tables of positions and magnitudes of stars in both fields are available from the first author.

4. Corrections for crowding

No reduction scheme can detect every star in a field. For the star counts produced by the procedure described in §3 to be meaningful, they must be corrected for the fraction of stars missed entirely, and for the fraction that are measured so poorly that they jump in or out of the magnitude range under consideration. Alternatively, the observed counts could be compared directly with a model of the density distribution in which these crowding effects had been included. Since we will use both strategies in §5 and §6, we first discuss the methods of correction here.

4.1. Artificial-star experiments

Artificial-star experiments, in which the images are re-reduced many times with a few artificial stars of known magnitude and position added each time, have become a standard technique for quantifying the effects of crowding in observations of star fields (e.g., incompleteness). Since our images were reduced entirely by software, performing many such experiments required minimal effort.

In each experiment, we added ~ 150 stars of random magnitude and position to each image, and re-reduced from scratch. (We ensured that the artificial stars added in a single experiment did not interfere with one another, by reselecting any position that was within 32 pixels of an artificial star that had already been added.) In the $r = 20''$ field, artificial stars were added at the same position in both B and V frames, with a color that would put the star on the main-sequence ridgeline. No color was needed for stars in the central field, since we did not use its B image.

After the images with artificial stars had been reduced, we recorded whether the artificial stars were recovered, and if so, their positions and magnitudes. We also recorded the positions and magnitudes of any *real* neighbor of the artificial stars. This latter step allowed us to investigate the blending of stellar images: if an artificial star happened to fall within 3 pixels of a real star, the two were sometimes identified as a single object by the reduction procedure. In such cases, we considered the object in the output list to be the *brighter* of the two. In other words, if the artificial star was brighter than its real neighbor, then the artificial star was recorded as having been recovered, with the magnitude of the blended object in the output list. On the other hand, if the artificial star was the fainter of the two, it was considered to have been lost. This scheme eliminates false large jumps in magnitude arising from misidentifications, and ensures that correction factors will be derived correctly by the matrix method described in §4.3.

In the central field, we wish to measure star counts (and, therefore, completeness statistics) as a function of both magnitude and position, which required us to analyze a large number of artificial stars ($\sim 6 \times 10^4$). For the $r = 20''$ image, we will obtain only one LF for the entire field, so a smaller number sufficed ($\sim 10^4$).

4.2. Causes of incompleteness

We may use the results of our artificial-star experiments in two ways. First, we could correct our *observed*, “raw” star counts for incompleteness, to obtain the *corrected* number of stars actually present. Alternatively, we could begin with a *model* of the true number of stars present (usually as a function of position or magnitude), and then test the model by using the artificial-star results to predict how many of those stars would be detected by our reduction procedure, and then comparing that prediction with the observed counts.

While the first approach is both more common and more straightforward, the statistical properties of the corrected counts that it produces make those counts difficult to use (§5.4). The second approach avoids these problems, but it requires an understanding of the reasons that some stars were detected while others were not, for adequate predictions to be made. Let us consider the two approaches.

First, correcting observed counts for incompleteness is quite simple: we use the artificial-star results to find a completeness fraction c , defined as the ratio of the number of artificial stars recovered in a given magnitude range to the number originally added in the same range, and then

correct the observed counts using c . For example, if we count 1000 stars in a region, and find a completeness fraction of 0.8, then our estimate for the true number of stars is $1000/0.8 = 1250$. The procedure can be generalized to handle multiple magnitude ranges, when measuring a luminosity function (§4.3).

On the other hand, suppose that we wish to use the other approach: that we have a cluster model that predicts the number of stars in some region, and that we want to use the artificial-star results to further predict how many of those stars we would actually detect, if we observed a cluster described by that model. When we use this approach in §5.5, the models will be density profiles (star counts as a function of radius), but for simplicity, let us consider here a model that consists of a given number of stars uniformly distributed over a region of the sky. Our goal, then, is to see whether the number of detectable stars is *incompatible* with our observed number of stars; if so, we can rule out the model in question.

For example, we might be interested in whether the region mentioned above could contain 1100 stars, rather than 1250. The region might be the central $2''$ of a globular cluster, and the difference between 1100 and 1250 stars might be the difference between the numbers of stars in a $2''$ core and in a cusp. In this case, we would want to know whether we could rule out the $2''$ core.

Now, we cannot turn our model’s total number of stars, 1100, into a prediction of the number we would detect, without an understanding of the *causes* of the incompleteness: the circumstances under which a particular star would or would not be found. To show this, let us look at two extreme cases, before discussing our actual M15 data.

In the first case, imagine that a few brighter stars appear in the real image, blocking our view of 20% of the (fainter) stars of interest (giving us $c = 0.8$). (Call this situation Case I.) In this case, we *know* those brighter stars’ positions, and thus know that they will block the *same* fraction of the fainter stars, no matter how many of the latter happen to be there. We can conclude that if 1100 fainter stars were present (as in our alternative model), then we would measure $1100 \times 0.8 = 880$ of them—a number quite different from our measurement of 1000 in the real image. If the difference were large enough, we might rule out the 1100-star model.

As a second case, though, imagine that the cause of the incompleteness was crowding of the faint stars themselves. In other words, suppose that 20% of the faint stars in the real 1250-star image happened to fall along the same line-of-sight as other faint stars, so that the resulting high fraction of blends lowered c to 0.8.

In this case—Case II—it is not clear what the completeness fraction would be if only 1100 stars were present, since the frequency of blends depends upon the stellar density. We might be tempted to apply the c of 0.8 to the 1100-star model, as in the previous case, but this would not be correct. Since an 1100-star image would be less crowded than the 1250-star image we have already analyzed, the appropriate c in the 1100-star case would be somewhat higher than 0.8. Unfortunately, *there is no way to know how much higher*, without running a new set of simulations of the reduction process with 1100-star artificial images.

Leaving aside the details of how one might do such simulations, suppose that they told us that the completeness fraction at the lower density was, say, 0.9. Our prediction would then be that we would detect $(1100)(0.9) = 990$ stars—almost exactly the number that we *did* detect in our actual image (1000).

So, is it possible to say which model fits better, in a Case II field: 1250 stars with 80% completeness, or 1100 stars with 90% completeness? While the predicted number of counts is nearly the same, the measurement of c *does* distinguish the two (specifically, the measured c of 0.8 is much lower than the 1100-star model’s 0.9).

The difficulty in rejecting the 1100-star model, though, is twofold. First, more work was required (an additional set of simulations). Second, the *significance* of the disagreement between the observed quantities and the ill-fitting model’s prediction is difficult to determine, because the uncertainty of the completeness fraction is not well known. There could easily be systematic differences between the real images and the simulations, since the latter would have to be created from scratch. (Artificial-star experiments, on the other hand, begin with the real image, so such differences would be much smaller.) In particular, the FOC’s nonlinearity and saturation would be very difficult to simulate realistically.

To sum up: Artificial-star experiments allow us to correct observed counts for incompleteness in *both* cases. They also allow us to incorporate incompleteness into a model, *if and only if* the incompleteness is similar to Case I (i.e., dominated by bright stars). In a region where blending of faint stars is important, artificial-star results cannot be applied to alternative models; incompleteness in those models must be simulated in some other way.

Before proceeding further, then, it is appropriate to determine which case applies to our M15 images, especially the innermost few arcseconds. Near the cluster center, the image is nearly covered by faint stars (see Fig. 3, and recall that the areas covered by saturated stars were excluded from analysis entirely), so one might wonder whether the region was more like Case II than Case I. However, we will show later that the region is actually closer to Case I than II: the incompleteness of the stellar sample we will use for profile-fitting is dominated by the effect of stars brighter than that sample (but not so bright as to be saturated). We will therefore go on to describe our methods for using the artificial-star results in more detail—knowing in advance that those results will not need to be replaced by an impractically large set of simulations when we fit models in §5.

4.3. Recovering the true LF from the data

To correct the raw star counts for crowding—in a more general case than the simple example given in the last section—we can proceed as follows: Let the true luminosity function (LF) of stars in an observed field be expressed as a vector T , where T_j is the number of stars observed in magnitude bin j . Let vector R be the “raw” LF: the number of stars that actually appear in each

bin of our photometry list. Two effects cause R to differ from T .

The first is scatter in the photometry: photon statistics and crowding cause stars to be measured brighter or fainter than their true magnitudes. In this case, features in the true LF T will be blurred in the observed LF R . This effect is sometimes called “bin-jumping”.

The matrix method of Drukier *et al.* (1988) allows us to correct for bin-jumping, and recover T from R . We use the output of our artificial-star experiments to construct a transition matrix A , where element A_{jk} measures the probability that a star whose true magnitude is in bin j will be measured to be in bin k . Once we have A , its inverse allows us to obtain T from R (i.e., since $R = A \cdot T$, $T = A^{-1} \cdot R$). Note that we need not “guess” any particular LF before running artificial-star experiments, since the absolute number of artificial stars in each bin never enters the calculation.

The second reason that R will differ from T is that some stars are entirely undetected by the reduction procedure—some blended with neighbors, and others lost in the noise. In this case, the raw LF R will need to be corrected upward to obtain T . Since such nondetections are also enumerated by artificial-star experiments, they can be incorporated into the transition matrix A (each column of A will sum to some value less than 1.0).

4.4. Comparison with previous work

GYSB found that their WFPC2 starcounts in the M15 cusp needed to be corrected *downwards*: they counted more stars than were actually present, down to $V = 19$. They attributed this effect to the fact that many of the “stars” they measured with magnitudes just above the limit were actually blends of two or more fainter stars, whose individual magnitudes were below the limit. We see no such effect (i.e., our counts need a slight upward correction, at the same magnitude limit). This difference most likely arises from the FOC’s higher resolving power: many of GYSB’s blends should be separated on our own images, and thus resolved as individual stars in our star list.

To make a quick check of this hypothesis, we simulated the WFPC2’s resolution, by assuming that any artificial star with a close real neighbor (within $0''.05$) would have been blended with that neighbor in GYSB’s images. We then recomputed completeness statistics, using the *combined* magnitude of the artificial star and its neighbor as the blend’s recovered magnitude. Enough artificial stars were “promoted” above $V = 19$ by this procedure that the completeness at that limit climbed above 100%—in other words, we recovered more stars with $V < 19$ than we originally added, exactly as seen by GYSB.

(The completeness calculated this way is not exactly the same as GYSB’s result, but we are not trying to duplicate the details of their work here—just identifying the source of the difference between our value of the completeness and theirs.)

5. Star-count analysis

5.1. The cluster center

Standard techniques for finding centers of clusters from star counts rely on finding the stars’ center of symmetry, in one way or another (see Calzetti *et al.* 1993, Sosin & King 1995, GYSB). Large sections of the FOC images are covered by saturated stars that are asymmetrically distributed around any prospective center, making a measurement of the center’s position impossible. We therefore use the position found by GYSB from their Planetary Camera image, which appears at pixel coordinates (284, 150) in the uppermost of the two FOC pointings that make up the field shown in Fig. 1. The position of the center is also marked in Fig. 3.

5.2. Binned star counts

Since the stellar surface density—and thus the crowding—changes dramatically over the inner $10''$ of M15, the limiting magnitude of our star counts varies widely with position in the central field. At its edge, $\sim 10''$ from the cluster center, we can accurately count stars down to nearly $V = 23$, while in the innermost arcsecond, crowding limits the completeness of the counts to $V \simeq 20$. (For comparison, GYSB’s limiting magnitude at the center was also $V \simeq 20$, although their completeness was less than 50% in the innermost $0''.5$. They did not attempt to push the counts to fainter magnitudes at larger radii.)

For the rest of §5, we divide the counts in the central field into three magnitude groups. The brightest (“turnoff”) sample contains all stars with $18.25 \leq V < 19.75$, the second (“middle”) group has $19.75 \leq V < 21.25$, and the third (“faint”) group has $21.25 \leq V < 22.75$. We require a completeness of $> 50\%$ for star counts to be considered believable. This implies that the turnoff group can be counted all the way into the center; stars in the middle group are countable in to $\sim 1''$, while the faint group can be counted only outside of $\sim 3''$. Within these ranges in radius, and before correction for incompleteness, there are 577 stars in the turnoff group, 1222 stars in the middle group, and 539 stars in the faint group.

If we assume an apparent distance modulus of 15.40 (DH93), the Bergbusch & Vandenberg (1992) isochrone discussed above tells us that our “middle” group consists of main-sequence stars with masses $0.67M_{\odot} < M < 0.77M_{\odot}$; for the “faint” sample, the mass range is $0.55M_{\odot} < M < 0.67M_{\odot}$. The “turnoff” sample consists of stars with masses $\sim 0.8M_{\odot}$; the range in mass of stars in this bin is much smaller than in the other two.

Figure 6 shows the completeness-corrected star counts in these three magnitude ranges, binned in radius. The raw (uncorrected) star counts are also shown, as the lines without circular points. To correct the raw counts for incompleteness, we used the Drukier method to compute a transition matrix for each radial bin and for each magnitude range, and corrected the counts appropriately (see §4.3). (We subdivided the counts into 0.5-mag bins in the construction of A ,

R , and T , and tabulated at least 1 mag on either side of each sample, to account for stars that jumped into and out of the magnitude range.) Note that the raw counts are occasionally greater than the corrected counts, as a result of bin-jumping. The corrected binned counts are also given in Table 1. (The r 's given in that table are the radii of the middle of each annulus in which the stars were binned.)

As has been found by several previous investigators, the counts of “turnoff” stars in Fig. 6 climb as a power law with slope ~ 0.7 . Whether they level off into a flat, constant-surface-density core within $2''$ will be discussed further below; for now, we note that both a pure power law and a $\sim 1''$ core appear to be equally plausible, while a $2''$ core appears much less likely. The counts of stars in the two fainter groups—never before resolved—show similar power-law behavior. Since the maximum-likelihood method presented in the next section provides more robust estimates of cusp slopes than would a fit to the binned counts, we defer discussion of these results until later.

5.3. Maximum-likelihood analysis of the density profile

A disadvantage of binned counts is that information is lost in the binning process. Since we have positions and magnitudes for each star, it is desirable to use all of this information simultaneously in finding a “best-fit” profile.

The maximum-likelihood (ML) method for density-profile fitting, which does use all of this information, was originally described by Sarazin (1980). If the counts of objects are complete, then any prospective surface-density model $f(r)$ can be regarded as a probability distribution of the position of any particular object, when f has been normalized to 1 over the area on the sky covered by the image. The log-likelihood of seeing the data (the N counts), given $f(r)$, is the sum

$$\log L = \sum_{j=1, N} \log f(r_j), \quad (1)$$

where r_j is the projected radius of star j . If we have a family of density models, then that model f that maximizes the likelihood function L is taken to be the “best-fitting” model. In particular, it has become common to fit the centers of globular clusters with the family of functions

$$f(r; \alpha, r_c) = \frac{1}{[1 + C_\alpha (r/r_c)^2]^{\alpha/2}}, \quad (2)$$

where the parameters α and r_c , respectively, are the asymptotic slope of the density cusp (for $r \gg r_c$), and the core radius, at which the projected density falls to half its central value. The constant C_α is chosen to make this true for any α :

$$C_\alpha = 2^{2/\alpha} - 1. \quad (3)$$

It is tempting to regard the likelihood function $L(\alpha, r_c)$ as a probability distribution of the parameters, and to infer confidence limits on these parameters directly from L . Strictly speaking,

L cannot give us a distribution of the parameters unless we take a Bayesian approach: if we assume a uniform prior distribution of models over some region in (α, r_c) space, then L is identical to the probability distribution of α and r_c over that region (after normalization). There could, however, be other reasonable assumptions for a prior distribution: for example, we might regard a core radius of $0.1''$ to be just as likely as a core radius of $1''$, in which case we should choose a prior that is distributed uniformly in $\log r_c$. For the purposes of this paper, though, we will assume the simpler case of a uniform prior in α and r_c .

5.4. Incorporating incompleteness into the ML method

The presence of incompleteness implies that the star counts actually observed will match a distribution $g(r)$ that has been adjusted for incompleteness, rather than the intrinsic distribution f . We should therefore fit the observed counts to g , and choose the f corresponding to the best-fitting g as our estimate of the density profile.

Why not correct the counts themselves, as we did with the binned counts, and compare those corrected counts with the f 's directly? The reason is that the statistics underlying the ML method depend upon the individual stellar positions being independent events, whose joint probability forms the likelihood function. Fitting to corrected counts would violate this assumption, since more than one corrected count would arise from a single detection. (For example, in a part of the image where the completeness was 0.5, L would be the probability of finding two stars at each detected stellar position. This is not what actually happened; moreover, it gives a high weight to parts of the image that were measured poorly.)

Now, consider for a moment that we have a set of f 's that are of interest—e.g., the set of cluster profiles defined by Eq. (2). To generate the g 's actually used in the ML fit, we must multiply each f by some factor at each radius to account for incompleteness. But, as discussed in §4.2, the process of finding the appropriate factors for some hypothetical model is not straightforward, since our artificial-star experiments give us those correction factors for our actual image, rather than for any hypothetical image.

Nevertheless, we can apply those same correction factors to our hypothetical models *if* we can show that the incompleteness was caused by brighter stars, rather than crowding of faint stars, so that the completeness factors would be independent of the f we are fitting. (The details of how the completeness was tabulated as a function of radius will be given in the next section; here we are more concerned with the reasons a particular star was or was not recovered.)

To do so, we looked at the artificial-star results for turnoff stars more closely. We noted that in the innermost $3''$, only $\sim 1/3$ of the non-recovered artificial stars had real stars in their own magnitude range as close neighbors. This suggested that only $\sim 1/3$ of the incompleteness of turnoff stars was due to blends with other turnoff stars, and that the remaining $2/3$ was due to somewhat brighter subgiants. A visual inspection of the locations of the non-recovered artificial

stars led us to a similar conclusion. (Note that even more obvious areas of saturation had already been excluded before this stage.)

For artificial stars in the other two samples (the “middle” and “faint” groups), blending with stars in their own magnitude range was quite rare. The incompleteness for these fainter main-sequence stars was caused entirely by turnoff stars and subgiants.

Since most of the incompleteness was due to brighter objects, we proceeded under the approximation that the incompleteness fraction measured at a given radius in our artificial-star experiments was appropriate for all prospective profiles (Case I from §4.2).

5.5. Radial dependence of the completeness fraction

We used the artificial-star results (§4.1) to find a completeness ratio $p_m(r)$ for each magnitude bin m . We defined this as

$$p_m(r) = \frac{\text{number of stars that are detected, in the magnitude range, and at radius } r}{\text{number of stars actually present, in the magnitude range, and at radius } r}.$$

To fit a density profile, then, we used the ML method (§5.3) to find the best-fitting $g(r) = p_m(r)f(r)$, where f is chosen from the set of functions $f(r; \alpha, r_c)$ defined in Eq. 2. As discussed in §4.2 and justified in §5.4, p_m was a function only of radius, and not of the density itself.

We used the same magnitude ranges in the ML fit as were defined in §5.2, but we needed to tabulate each p_m as a function of r without an arbitrary binning in radius. From our completeness experiments, we had a database of $\sim 6 \times 10^4$ artificial stars. At the radius r of each real star, we found the N_a artificial stars nearest in radius to r (we chose N_a to be 1000 for the turnoff group, and 3000 for the fainter groups). The positions of the N_a artificial stars in this subsample defined an annulus, with midpoint r and width $\sim 1''$. Next, we constructed the transition matrix A for the subsample (see §4.3). We then tabulated the local raw LF vector R for the real stars that fell in the same annulus as the subsample, and applied A^{-1} to R to obtain the local true LF T . Finally, we found each $p_m(r)$ as the ratio of the sums of the appropriate elements of R and T . This method ensured that for each real star the p_m term used in the likelihood function was the most appropriate value at its position; no radial binning was necessary. Note also that p_m depends on the number of *real* stars, not just the artificial stars, since the artificial-star results must be weighted by the local LF in the computation of the overall completeness.

For stars at small radii (in the turnoff sample), for which there are fewer than N_a artificial stars within r , we replaced the annulus with a circle of radius $2r$. This allowed us to track the changes in p_m within the innermost arcsecond. The circle was never allowed to have fewer than 250 artificial stars in it. We also ignored the region within $0''.3$ of the cluster center, because the precise position of the center is not known, and because small-number statistics begin to dominate p_m .

The computed $p_m(r)$ is quite noisy. One reason is that the number of real stars within the annulus varies with r (since the local raw LF R is used in the computation of p_m , noise in R leads to fluctuations in p_m). A less important source of noise is the fact that the off-diagonal elements in the transition matrix A , which correspond to rare, large jumps in magnitude, are not well sampled. The high-frequency fluctuations in p_m lead to problems in the ML fit, since the product $p_m(r)f(r)$ must be normalized over the field of view; the noise makes the integrator take far too many steps. We therefore applied a second-order Savitzky–Golay smoothing filter (Press *et al.* 1992) with a smoothing length of 100 stars to the raw $p_m(r)$, to generate the p_m actually used in the profile fitting. (The second-order Savitzky–Golay filter preserves second-order moments, so that peaks or troughs in p_m will not be smoothed out.)

The smoothed $p_m(r)$ for each of the three stellar samples is shown in Figure 7. (In this section we concentrate on the turnoff sample; we will discuss the other two in §6.)

Note that $p_m(r)$ still fluctuates on radial scales shorter than the variations in the density profile. More smoothing would remove the remaining fluctuations, but not without losing resolution of features in $p_m(r)$ near the cluster center; we therefore decided not to smooth p_m any further. We did check the behavior of the ML fit with greater smoothing, and found that the results were essentially identical to what we will present, except that the smoothing made the measured core radius artificially large.

(An alternative method, suggested by the referee, would be to fit an analytic function to p_m . The danger in such a method is that the assumed functional form itself might determine the behavior of p_m at small radii, and thereby influence whether we deduce the presence of a small core. For example, the analytic function used by GYSB [their Eq. 2] *must* approach $1 + C_1 + C_2$ near $r = 0$. The values of C_1 and C_2 are set by fits at $r > 1''.5$, where the crowding conditions are quite different.)

The completeness of the turnoff sample is ~ 1 over most of the central field. It drops to ~ 0.5 only in the central arcsecond.

5.6. The density profile of the turnoff sample

We then fit the star counts in the turnoff sample to the family of f 's defined in §5.3, and obtain the log-likelihood function shown in Figure 8. The contour lines in Fig. 8 are plotted in steps of 1, so that a model that lies on the -2 contour is one-tenth as likely to produce the observed counts as a model that lies on the -1 line.

The likelihood function reaches its maximum at a cusp slope of -0.70 , and at a very small core radius. However, models with core radii up to $\sim 1''$ yield fits of essentially the same quality as the maximum-likelihood model; taken at face value, the 95% upper limit on r_c is $\sim 1''.3$. Assuming a flat prior, the one-sigma uncertainty of the slope α is ~ 0.05 , and its 95% confidence limits are

± 0.09 . This result is fairly consistent with previous values: GYSB’s result was -0.82 for a similar sample, with a 95% confidence limit of ± 0.12 .

It is important to realize that the cusp’s rise in the inner $2''$ is almost entirely due to the sharp drop in the completeness fraction p , and not to the uncorrected stellar density, which is roughly constant within $r = 2''$. (Again, GYSB’s study is similar: for $V < 20$ their uncorrected density is flat within $r = 3''$.) A better determination of an upper limit on r_c would require extensive and difficult simulations (see §4.2). Nevertheless, we believe that our upper limit on r_c is unlikely to be significantly in error, although the effect of properly accounting for faint-star blends would be to make it somewhat larger (perhaps $\sim 1''.5$). In any case, our results are not consistent with the presence of a $2''.2$ core, as claimed by Lauer *et al.* (1991). We do caution that the interpretation of maximum-likelihood fits to completeness-corrected star counts is not as straightforward as one might think.

5.7. Fainter stars in the cusp

The density profile of lower-mass stars in the central cusp of a globular cluster has never been observed. While the cusp is usually assumed to be the result of gravothermal core collapse, the presence of a black hole with a mass of $\sim 10^3 M_\odot$ has never been ruled out. Observations of lower-mass stars can test whether the cluster potential has the radial dependence predicted by core-collapse or by black-hole models.

In comparing cusp slopes of different stellar groups, we must choose a consistent radial range over which to measure the slopes. We might choose a range over which all groups are at least 50% complete (as in Fig. 6). This is a common requirement; it is intended to prevent small systematic errors in artificial-star experiments from dominating the corrected counts. However, in our case, we are interested in the *variation* of the corrected density with radius. This variation depends on dp_m/dr as well as on p_m itself, implying that systematic errors in the former can affect the deduced cusp slope just as much as systematic errors in the latter. For example, if there were multiple causes of incompleteness whose relative importance varies with density (and, therefore, position), and if we did not account for one of those effects correctly, then our measurement of the cusp slope would be strongly influenced by the completeness corrections, despite the fact that p_m was always over 50%.

This observation suggests that we set an upper limit on $|dp_m/dr|$, in addition to our p_m requirement, when measuring cusp slopes. But, since dp_m/dr is difficult to measure directly, we take a less formal approach, and simply choose to measure slopes in regions where p_m varies reasonably slowly with r , for each group (see Fig. 7, and ignore the small-scale fluctuations). Typically, c decreases slowly with decreasing r at large radii, and then drops dramatically at some radius—near $1''$ for the turnoff group, and $2''$ for the middle group. For the faint group, p_m varies rapidly with r over the entire central field, meaning that the accuracy of its radial profile depends

strongly on the absence of any systematic errors in the artificial-star procedure. (The *total* number of faint stars in the outer part of the central field is better known, since it depends only on an average p_m .)

The upper panel of Figure 9 shows the likelihood function of cusp slopes for the three stellar samples. To allow us to compare the slopes of the turnoff and middle groups, and to minimize the influence of any flat core on these fits, we ignored stars at radii less than $2''$, and fit the counts with essentially pure power laws ($r_c \rightarrow 0$ in Eq. 2). (For the faint group, the inner radial limit was $r = 3''$, the radius where its completeness climbs above 50%.) The lower panel of Fig. 9 shows the likelihood functions in a cumulative form. If we assume a uniform prior (see §5.3), this panel shows the probability of the cusp slope being flatter than a given value.

The solid line refers to the turnoff sample; its best-fit cusp slope here is -0.64 ± 0.08 . The dotted line is the middle group; its slope is -0.56 ± 0.05 . (The value for the turnoff group is flatter than the value found in the previous section, because we are using only stars with $r > 2''$, rather than $r > 0''.3$. In Fig. 6, one can see that the profiles of both groups steepen a bit near $r = 2''$. If we set the inner radial limit at $1''$ instead, these slopes become -0.67 and -0.64 , respectively.) The dashed line in Fig. 9 is the faint group; at face value it appears to decline very steeply (-0.8 ± 0.1). However, this last slope is dominated by the radial variation of the completeness correction, and probably should not be trusted.

What do models of the density cusp predict for the variation of cusp slope with stellar mass? Let $-\beta$ be the cusp slope in *space* density, so that the (negative) slope of the surface-density profile is $\alpha = \beta - 1$ (for $\beta > 1$). Models of clusters in the process of core-collapse (Cohn 1985) predict a strong variation of β with mass:

$$\beta_{cc} = 1.89 \left(\frac{m}{m_{\max}} \right) + 0.35,$$

where m_{\max} is the mass of the stars that dominate the cusp. These models also predict a space-density slope of $\beta \simeq 2.23$ for the dominant stars, which corresponds to a surface-density slope of $\alpha \simeq 1.23$ (Cohn 1980). The potential well in the cusp varies as $\Phi(r) = GM/r \propto r^{2-\beta} \propto r^{-0.23}$, assuming that it is dominated by the heaviest stars.

For the $0.8M_\odot$ turnoff stars to have $\alpha \simeq 0.64$ in a collapsing model, we must hypothesize the existence of a population of dark objects with masses near $1.2M_\odot$, or some combination of populations whose effect is similar. Such a model would predict slopes $\alpha \simeq 0.48$ and 0.32 for our two fainter groups, taking their mean masses to be 0.7 and $0.6M_\odot$. An isothermal cusp in thermodynamic equilibrium, which might be a more appropriate model of the post-core-collapse phase, would predict slightly flatter slopes (0.44 and 0.23 , respectively).

Black-hole models, on the other hand, predict far less variation of cusp slope with stellar mass (Bahcall & Wolf 1977), since the potential well is much steeper in the BH case: r^{-1} rather than $r^{-0.23}$. The BH models predict $\alpha = 0.75$ for the most massive stars in the cusp (the turnoff stars, in this case), with a slow variation of slope with stellar mass, down to ~ 0.5 for very-low-mass

stars. Over the range of masses covered by our observations, the difference in slope should be negligible; all three groups should have slopes near 0.7.

The turnoff group’s slope is consistent with either the core collapse model (assuming heavy remnants are present), or the black hole model (the slope is within 1.0 or 1.4σ of -0.75 , depending on which radial range is adopted). The middle group’s slope measured here, though, falls between the predictions of the two models. From Fig. 9, the probability of the slope being ≤ 0.48 (the core-collapse prediction) is about 7%; while the probability of its being ≥ 0.7 is only about 1%.

Overall, the core-collapse model is somewhat more consistent with these data than is the black-hole model, although neither can be considered a very good fit. However, it should be noted that the cusp slopes seen by Chernoff & Weinberg (1990) in their Fokker–Planck simulations did not always agree with the Cohn (1985) prediction, so true evolving core-collapse models may match these observations more closely.

6. Mass segregation

From the V magnitudes of stars in the central and $r = 20''$ fields, we derive the luminosity functions shown in Figure 10. (The uppermost LF refers to the same stars that were discussed in §5, but we now plot them as a luminosity function, instead of a surface-density profile.) The LFs have been corrected for incompleteness and “bin-jumping” by the Drukier matrix method (see §4.3). We plot the central field LF down to $V = 22$, for $3'' < r < 8''$. Note that the *total* number of faint stars in the indicated radial range is not affected by the uncertainties in dp_m/dr that made the determination of their radial profile difficult, so the caveats from §5.7 do not apply to Fig. 10 (or to Fig. 11 below).

We next convert magnitudes to masses using the $[\text{Fe}/\text{H}] = -2.26$, $t = 15$ Gyr isochrone of BV92 (the isochrone plotted in Fig. 5). The best choice of mass-luminosity relation is a matter of some debate, but we are concerned with stars with masses above $0.5M_\odot$, for which the differences between M–L relations are minor. We choose the BV92 isochrone because it reproduces the magnitudes and colors near the main-sequence turnoff quite well (DH93); more recent calculations that fit the lower main sequence have not attempted to reproduce the turnoff.

We plot the resulting mass functions in Figure 11, along with the MF recently measured by Piotto *et al.* (1996) in a field $5'$ from the center of M15, using the WFPC2 on *HST*. The two FOC MFs refer to the left-hand scale, while the WFPC2 MF refers to the right-hand scale. The stellar density is much lower in the $r = 5'$ field; the vertical position of the WFPC2 MF has been chosen to match the $r = 20''$ MF at the bright end, so that the two may be easily compared. The MFs are also given in Table 2.

The $r = 20''$ and $r = 5'$ (WFPC2) MFs clearly show substantial mass segregation; the former is much flatter than the latter. (Note that differences between the V filters used in the WFPC2

and FOC are minor, and certainly could not account for the difference in MFs.) Their difference is in the direction one would expect from two-body relaxation. The innermost MF continues this trend, with even fewer low-mass stars.

A quantitative, model-independent measurement of the degree of mass segregation is difficult: the three MFs do not cover the same mass range, and none of the MFs are well fit by power laws. Nevertheless, we can compare rough power-law slopes over various ranges of mass. Over the range from the turnoff ($0.78M_{\odot}$) to $0.45M_{\odot}$, the $r = 5'$ WFPC2 MF is best fit by a power-law with a slope $x = 1.00 \pm 0.25$ (where the Salpeter slope is 1.35); this power-law slope is in excellent agreement with the results of DH93 over a similar mass range. The $r = 20''$ MF is best fit by $x = -0.75 \pm 0.26$ over the same range; the two are therefore different at the $\sim 5\sigma$ level.

Considering only the range in mass from 0.78 to $0.60M_{\odot}$, for which data in all three radial bins are available, we measure a slope $x = 2.1 \pm 1.0$ for the $r = 5'$ field, $x = 0.2 \pm 0.7$ for the $r = 20''$ field, and $x = -2.2 \pm 0.4$ for the $3'' < r < 8''$ sample. In this case, the last two slopes differ at the 3σ level.

Computational simulations of globular-cluster evolution have usually assumed a power-law mass function, so a comparison with theory also requires us to choose a mass range. Grabhorn *et al.* (1992) constructed a Fokker–Planck model of M15 with a global MF slope of $x_{\text{global}} = 0.9$ —quite close to the measured value at $r = 5'$ over the first of the two mass ranges considered above. Figure 8 of Grabhorn *et al.* shows the radial variation of the MF slope at the time of deep core collapse in their model; from that plot, $x = 1.2$ at $r = 5'$, $x = 0.1$ at $r = 20''$ and $x = -0.4$ at $r \simeq 5''$. The differences between these slopes appear to be smaller in the model than in our observations. If this particular “snapshot” of the model is appropriate for comparison with M15 at the present epoch, then the model is underestimating the degree of mass segregation in the cluster.

(Note that here we are comparing the *overall* MF of each field with the others. Within the central cusp itself, the Fokker–Planck models *overestimate* the radial variation of the MF [§5.7].)

Drukier (1995) has recently constructed an evolving Fokker–Planck model of the cluster NGC 6397, which he could compare with the observed surface-density profile and mass functions at many stages of the calculation. The data presented in this paper should be useful for similar comparisons with evolutionary models of M15.

7. A King–Michie model of M15

Lacking the resources to run a Fokker–Planck or N -body model of M15, we instead constructed a multimass King–Michie model. Such models do not include many of the physical processes that make M15 such an interesting object to study (e.g., core collapse), but are the simplest models that can give a somewhat realistic prediction of the variation of the mass function throughout the entire cluster, including the region near the tidal boundary. They are also easy to

calculate, and are a first step with which more sophisticated models can be compared.

The hallmark of the King–Michie model is its “lowered Maxwellian” distribution function (DF); the DF goes to zero at the cluster’s escape energy. King (1965) showed that this DF approximates the steady-state solution of the Fokker–Planck equation; the first actual models were calculated by Michie & Bodenheimer (1963) and King (1966). The most general form of the models, which includes anisotropy of the velocity dispersion and multiple stellar mass groups, was published by Gunn & Griffin (1979). The code used to calculate the model presented here uses the notation and technique of Gunn & Griffin.

To calculate a model, we first specify a set of mass groups. We choose a mean mass for each group, and some constraint on the number of stars in the group—either the total number of stars, or the projected stellar density at some radius (which is usually chosen to agree with an observed mass function). We then supply the desired core, tidal, and anisotropy radii, which are chosen so that the model’s density profile agrees with observation. The code then iterates for a model with the chosen set of parameters. After the model has been computed, we can check its predicted stellar velocities and mass segregation against observation.

For the model presented here, we chose a tidal radius r_t of 60 parsecs and a core radius r_c of 0.01 pc = 0''.2; the small r_c allows the model’s density cusp to continue in to small radii. Values of r_c up to 0.1 pc lead to models with virtually the same predictions; the only difference is that the density profile flattens near the innermost density points. We also used an anisotropy radius, r_a , of 22 pc = 7'.3 (the stellar velocities become increasingly radial beyond r_a). We were unable to fit the density profile well with any model with isotropic velocities; the surface-density profile of the best-fitting isotropic models fell below the observed profile in the “shoulder” around $r = 20''$.

The model’s mass function consisted of 15 groups. The first 13 groups were constrained to agree with the observed WFPC2 mass function at $r = 5'$. Group 14 contained white dwarfs, with a mean mass of $0.55 M_\odot$. The number of WDs was chosen so that $\sim 20\%$ of the cluster mass was in WDs, in rough agreement with various other models that have been calculated (e.g., Meylan & Mayor 1991). The WD mass fraction could be varied between 10% and 30% without affecting the model dramatically.

Group 15 contained massive, dark stellar remnants—neutron stars or heavy WDs. Since these stars are the heaviest objects in the model, they concentrate strongly toward the cluster center, and control the inner density profile of the luminous giants. As in the core-collapse models discussed in the previous section, the *individual* mass of the heavy remnants determines the slope of the density cusp of the turnoff stars, while their *total* mass determines the cusp’s radial extent. To match the cusp, then, we put ~ 1800 $1.5M_\odot$ stars into Group 15, which constituted 0.78% of the total cluster mass of $3.4 \times 10^5 M_\odot$. (The cusp extends to about $10''$, although the heavy remnants dominated the total mass density out to a radius of only $2''$ or so.) It is interesting that the best-fit remnant mass is quite close to the Chandrasekhar mass ($1.44M_\odot$).

(Some other pre-*HST* cluster modeling has taken the approach of varying the MF power-law

slope until a model can be found that agrees with observations; since the number of remnants in those models is set by an extrapolation of the MF slope, the procedure is essentially similar to ours. In our case, since we now know the main-sequence MF from observation, we must adjust the number of remnants independently.)

One might criticize the model on the grounds that it is rather *ad hoc*. For instance, the numbers of WDs and heavy remnants are not necessarily consistent with an extrapolation of the chosen MF. Furthermore, the anisotropy radius was regarded as a free parameter; another procedure might have been to *require* r_a to be equal to the radius at which the relaxation time is equal to the cluster’s age (the two did turn out to be within about a factor of two of each other). However, our goal here is to see whether any King–Michie model can adequately *describe* the observed state of the cluster; we leave the interpretation of any successful fits for another time.

The comparison of the model with observed quantities is shown in Figure 12. (The model parameters and mass functions are listed in Tables 3a and 3b.) The lower right panel shows the mass function at $r = 5'$ as measured by Piotto *et al.* (1996) and as it appears in the model output. Their similarity confirms that the iteration procedure successfully matched its constraints. (Note that the model’s mass function does not *exactly* match the measured MF. The MF used in the model was rounded off to even quantities, to avoid unnecessary scatter in the plotted points.)

The upper left panel of Fig. 12 shows the projected surface density profile. The line is the model output, which was matched to the plotted points. The heavy points are the turnoff stars’ profile from Fig. 6, and the lighter points are ground-based observations from Lugger *et al.* (1987) and King *et al.* (1968). The lower part of this panel shows the logarithmic difference between the surface-density data and the model.

The upper right panel of Fig. 12 compares the predicted and observed inner mass functions; the plotted points are identical to those shown in Fig. 11. The solid lines are the model predictions. The predicted MF for $3'' < r < 8''$ has been averaged over the area of the central field, so that it can be compared directly with the observed MF. Unlike the Fokker–Planck models, the King–Michie model predicts *stronger* mass segregation than is actually observed: both model lines go down with decreasing mass faster than the data. (The amount of disagreement is somewhat sensitive to details of the assumed $r = 5'$ MF, in particular, to the slope of the MF’s rise near $\log m = -0.2$. But no such adjustments could make all of the predicted MFs consistent with observation.)

Finally, the lower left panel of Fig. 12 shows the model-predicted velocity dispersion profile, along with the binned velocity dispersion profiles of Peterson, Seitzer, & Cudworth (1989, plotted as squares) and Gebhardt *et al.* (1994, plotted as triangles). (The questionable innermost point of the Peterson *et al.* profile is not shown.) Like other high-concentration King–Michie models, the model shown here is nearly isothermal in its center, and does not reproduce the rise in M15’s velocity dispersion in the inner $30''$.

The Grabhorn *et al.* (1992) Fokker–Planck model of M15 *does* reproduce the velocity profile,

at least more closely: core-collapse models have a power-law dependence of the velocity dispersion on radius, with logarithmic slope -0.23 . The Grabhorn model also fit the cluster with a much larger fraction of heavy remnants (9% of the cluster mass, rather than 0.8%), which brought their *central* velocity into agreement with the accepted observational value of $\sim 14 \text{ km s}^{-1}$ (Dubath, Meylan, & Mayor 1994). Putting such a high fraction of heavy remnants into the King–Michie model would allow the central velocity dispersion to agree with observation, but not the run of velocity dispersion with radius. The agreement of the density profile with observation would also be destroyed.

In summary, we can fit a King–Michie model to the observed mass function and surface-density profile of M15, but the model does not fully reproduce the observed degree of mass segregation. Since King models were already known not to fit the stellar velocities (Grabhorn *et al.* 1992, Gebhardt & Fischer 1995), this lack of agreement is not a surprise. However, our model is the first to use the actual observed cluster MFs, and thus confirms that M15 is not in dynamical equilibrium.

8. Conclusions

We have presented radial distributions and mass functions of main-sequence stars in two fields near the center of M15. The distribution of turnoff stars in the innermost $10''$ is similar to what has been found previously: we find a power-law density cusp, with logarithmic slope -0.70 ± 0.05 (for stars with $r > 0''.3$). The density continues to rise in to small radii; any constant-surface-density core must be smaller than $1''.5$.

We have shown, for the first time, that fainter, lower-mass stars also have a power-law distribution near the cluster center; we find a logarithmic slope of -0.56 ± 0.03 for a group of stars with masses near $0.7M_{\odot}$, over the radial range from $2''$ to $10''$. (Over the same range, turnoff-mass stars have a slope of -0.64 ± 0.08 .) These slopes are not well matched by the predictions of the simplest core-collapse and black-hole models.

We have also compared the mass functions in our fields with the MF in a field $5'$ from the cluster center, and found a strong degree of mass segregation. Finally, we fit a King–Michie model to the cluster’s surface-density profile and outer mass function, and showed that it predicts somewhat less segregation than we observe. The model also does not match the cluster’s velocity-dispersion profile.

While our observations alone cannot settle the debate over the dynamical state of M15, we hope our results will provide a valuable set of inputs to a new generation of sophisticated and realistic models of globular-cluster evolution.

It is a pleasure to thank Jay Anderson, Aaron Barth, Adrienne Cool, and George Djorgovski

for a number of suggestions in the course of this project, and Charles Bartels for computer assistance. We also thank an anonymous referee for many helpful comments. This work was supported by NASA grant NAG5-1607.

REFERENCES

- Bahcall, J. N., & Wolf, R. A. 1976, *ApJ*, 209, 214
- Bahcall, J. N., & Wolf, R. A. 1977, *ApJ*, 216, 883
- Bergbusch, P. A., & Vandenberg, D. A. 1992, *ApJS*, 81, 163 (BV92)
- Bolte, M. 1989, *ApJ*, 341, 168
- Calzetti, D., De Marchi, G., Paresce, F., & Shara, M. 1993, *ApJ*, 402, 1
- Chernoff, D. F., & Weinberg, M. D. 1990, *ApJ*, 351, 121
- Cohn, H. 1980, *ApJ*, 242, 765
- Cohn, H. 1985, in *Dynamics of Star Clusters*, eds. J. Goodman & P. Hut, p. 161
- De Marchi, G., & Paresce, F. 1996, “Very Blue Stars and Mass Segregation in the Core of M15”, preprint
- Djorgovski, S., & King, I. R. 1984, 277, L49
- Drukier, G. A., Fahlman, G. G., Richer, H. B., & Vandenberg, D. A. 1988, *AJ*, 95, 1415
- Drukier, G. A. 1995, *ApJS*, 100, 347
- Dubath, P., Meylan, G., & Mayor, M. 1994, *ApJ*, 426, 192
- Durrell, P. R., & Harris, W. E. 1993, *AJ*, 105, 1420 (DH93)
- Gebhardt, K., & Fischer, P. 1995, *AJ*, 109, 209
- Gebhardt, K., Pryor, C., Williams, T. B., & Hesser, J. E. 1994, *AJ*, 107, 2067
- Grabhorn, R. P., Cohn, H. N., Lugger, P. M., & Murphy, B. W. 1992, *ApJ*, 392, 86
- Greenfield, P. *et al.* 1991, *Proc. SPIE*, 1494, 16
- Guhathakurta, P., Yanny, B., Schneider, D. P., & Bahcall, J. N. 1996, *AJ*, 111, 267 (GYSB)
- Gunn, J. E., & Griffin, R. E. 1979, *AJ*, 84, 752
- Hut, P., & Makino, J. 1996, eds., “Dynamical Evolution of Globular Clusters: Confrontation of Theory and Observation” (IAU Symp. 174)
- Jedrzejewski, R. I., Hartig, G., Jakobsen, P., Crocker, J. H., & Ford, H. C. 1994, *ApJ*, 435, 7L
- King, I. R. 1965, *AJ*, 70, 376
- King, I. R. 1966, *AJ*, 71, 64
- King, I. R., Hedemann, E., Hodge, S. M., & White, R. E. 1968, *AJ*, 73, 456
- King, I. R., Anderson, J., & Sosin, C. 1994b, in *Calibrating Hubble Space Telescope: Proceedings of a Workshop Held at STScI*, eds. J.C. Blades & S.J. Osmer (Baltimore: STScI), p. 130
- Lauer, T. R. *et al.*, *ApJ*, 369, L45
- Lugger, P. M., Cohn, H., Grindlay, J. E., Bailyn, C. D., & Hertz, P. 1987, *ApJ*, 320, 482

- Meylan, G., & Mayor, M. 1991, *A&A*, 250, 113
- Michie, R. W., & Bodenheimer, P. 1963, *MNRAS*, 126, 269
- Peterson, R. C., Seitzer, P., & Cudworth, K. M. 1989, *ApJ*, 347, 251
- Piotto, G., Cool, A. M., & King, I. R. 1996, “A Comparison of Deep *HST* Luminosity Functions”, submitted to *AJ*
- Press, W. H., Teukolsky, S. A., Vetterling, W. T., & Flannery, B. P. 1992, *Numerical Recipes: The Art of Scientific Computing*, Second Edition (Cambridge: Cambridge University Press)
- Sarazin, C. 1980, *ApJ*, 236, 75
- Sosin, C., & King, I. R. 1995, *AJ*, 109, 639
- Stetson, P. 1987, *PASP*, 99, 191
- Stetson, P. 1992, in *Astronomical Data Analysis Software*, ed. D. M. Worrall, C. Biemesderfer, and J. Barnes (ASP Conference Series, Vol. 25), p. 297
- Yanny, B., Guhathakurta, P., Bahcall, J. N. & Schneider, D. P. 1994, *AJ*, 107, 1745

Fig. 1.— F480LP (FOC “V”) image of a 13.6×7.2 -arcsecond region near the center of M15. The cluster center is near the middle of the figure.

Fig. 2.— F480LP (FOC “V”) image of a 7×7 -arcsecond region, 20 arcsec from the center of M15. The scale is twice as large as in the previous figure. The circle indicates the position of the blue star described in §3.2.

Fig. 3.— F480LP (FOC “V”) image of the innermost $3''.5 \times 3''.5$ of M15. The cross marks the position of the cluster center as found by GYSB (see §5.1). Note the diffraction rings around the images of stars, and the severe crowding in the innermost $\sim 1''$. Stars of various V magnitudes are indicated. The large crescent-shaped regions are badly saturated bright stars.

Fig. 4.— An illustration of the image reductions. The five panels show the same small section of the central field at different stages of the reduction process. From left to right: (a) in the original image, (b) after the first pass, (c) after diffraction rings have been removed using the first-pass results, (d) after the second pass, (e) the final subtracted image.

Fig. 5.— A color–magnitude diagram, in Johnson B and V , of the $r = 20''$ field. The solid line is the 15 Gyr, $Z = 10^{-4}$ isochrone of Bergbusch & Vandenberg (1992), and the dashed line is the fiducial main sequence of Durrell & Harris (1993). The deviation of the points from the lines at the bright end is a result of detector nonlinearity in the B image (see the text).

Fig. 6.— The projected stellar density in the inner $10''$, plotted in radial bins, in three magnitude ranges. The circular points connected by lines refer to the counts corrected for incompleteness. The lines without points show the “raw” counts, prior to correction.

Fig. 7.— The completeness ratio $p_m(r)$ for the three stellar samples. See the text for an explanation of the fluctuations.

Fig. 8.— The log-likelihood of the “turnoff” sample ($18.25 < V < 19.75$), as a function of the cusp slope α and core radius r_c in arcseconds, using the fitting function defined by Eq. 2. Lighter areas indicate a higher probability of seeing the observed counts. Contour lines are plotted one unit apart, so that each line represents a factor of 10 in the likelihood function. Thus, a model with an (α, r_c) pair that lies on the -2 contour line is one-tenth as likely to produce the observed counts as a model whose (α, r_c) lies on the -1 line. The point of maximum likelihood lies at $\alpha = 0.7$ and very small r_c .

Fig. 9.— (Upper panel) The likelihood of seeing the observed counts as a function of the cusp slope α , for each of the three stellar samples, using the fitting function defined by Eq. 2. The solid curve refers to the turnoff magnitude bin ($18.25 < V < 19.75$), the dotted curve to the middle bin ($19.75 < V < 21.25$), and the dashed curve to the faint bin ($21.25 < V < 22.75$). (Lower panel) The same likelihood functions converted to a cumulative probability, assuming a uniform prior.

Fig. 10.— Luminosity functions in the central field and the $r = 20''$ field.

Fig. 11.— Mass functions in the central field and the $r = 20''$ field.

Fig. 12.— The King–Michie model, fit to our observations and to others from the literature. In all panels, points are observations, and solid lines are model constraints or predictions. (UL) The surface-density profile (model constrained to fit the observations). Inner points are from this work; outer points are from Luggner *et al.* (1987) and King *et al.* (1968). (LL) The velocity-dispersion profile (model does not reproduce the central rise in velocity dispersion). Points taken from Peterson, Seitzer, & Cudworth (1989, plotted as squares), and Gebhardt *et al.* (1994, plotted as triangles). (LR) The mass function at $r = 5'$ (model constrained to fit the data), from Piotto *et al.* (1996). (UR) Mass functions in the central and $r = 20''$ fields (model predicts stronger mass segregation than observed, when compared with $r = 5'$ field), from this work.

Figure 1

Figure 2

Figure 3

a b c d e

Figure 4

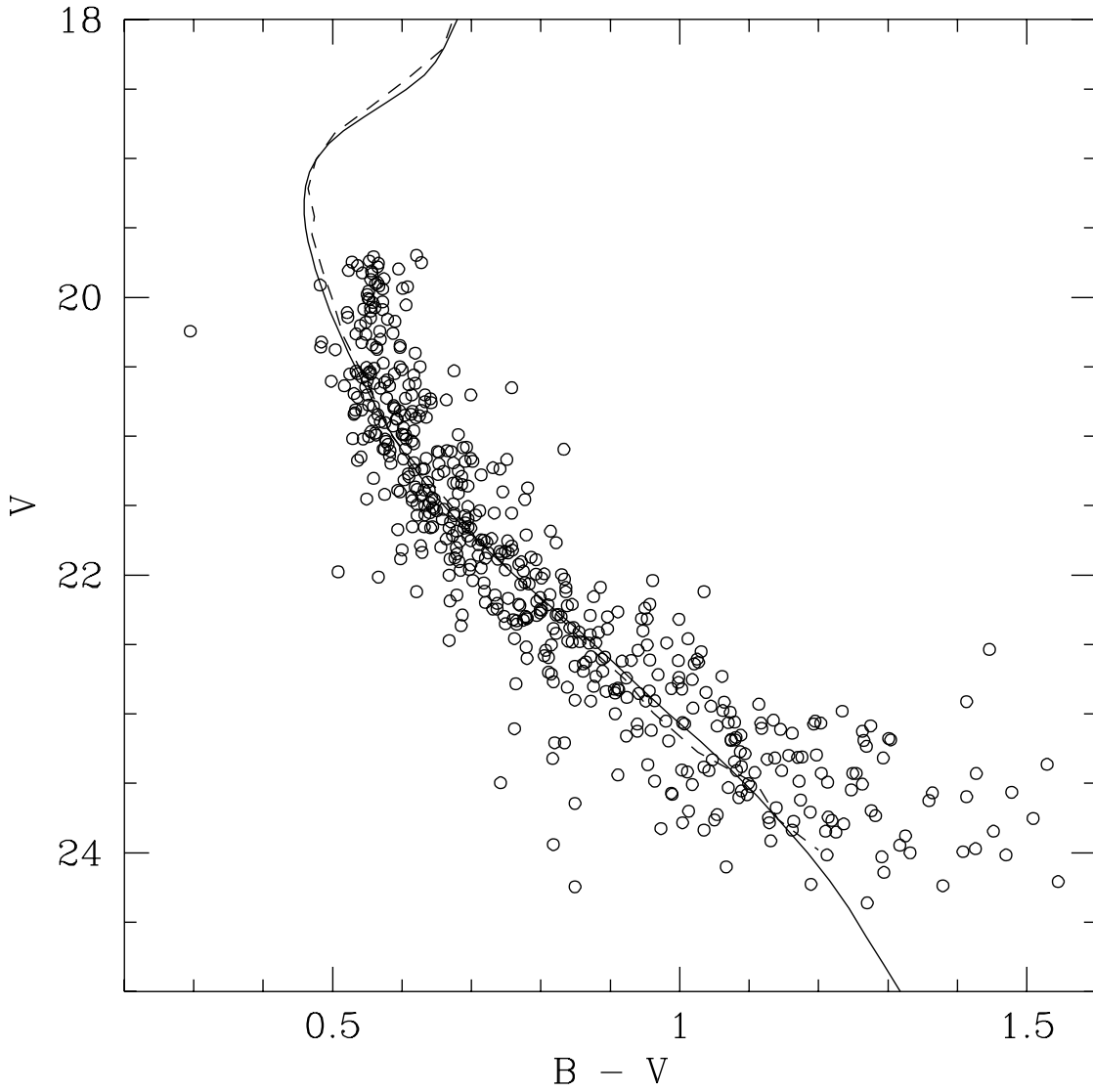


Figure 5

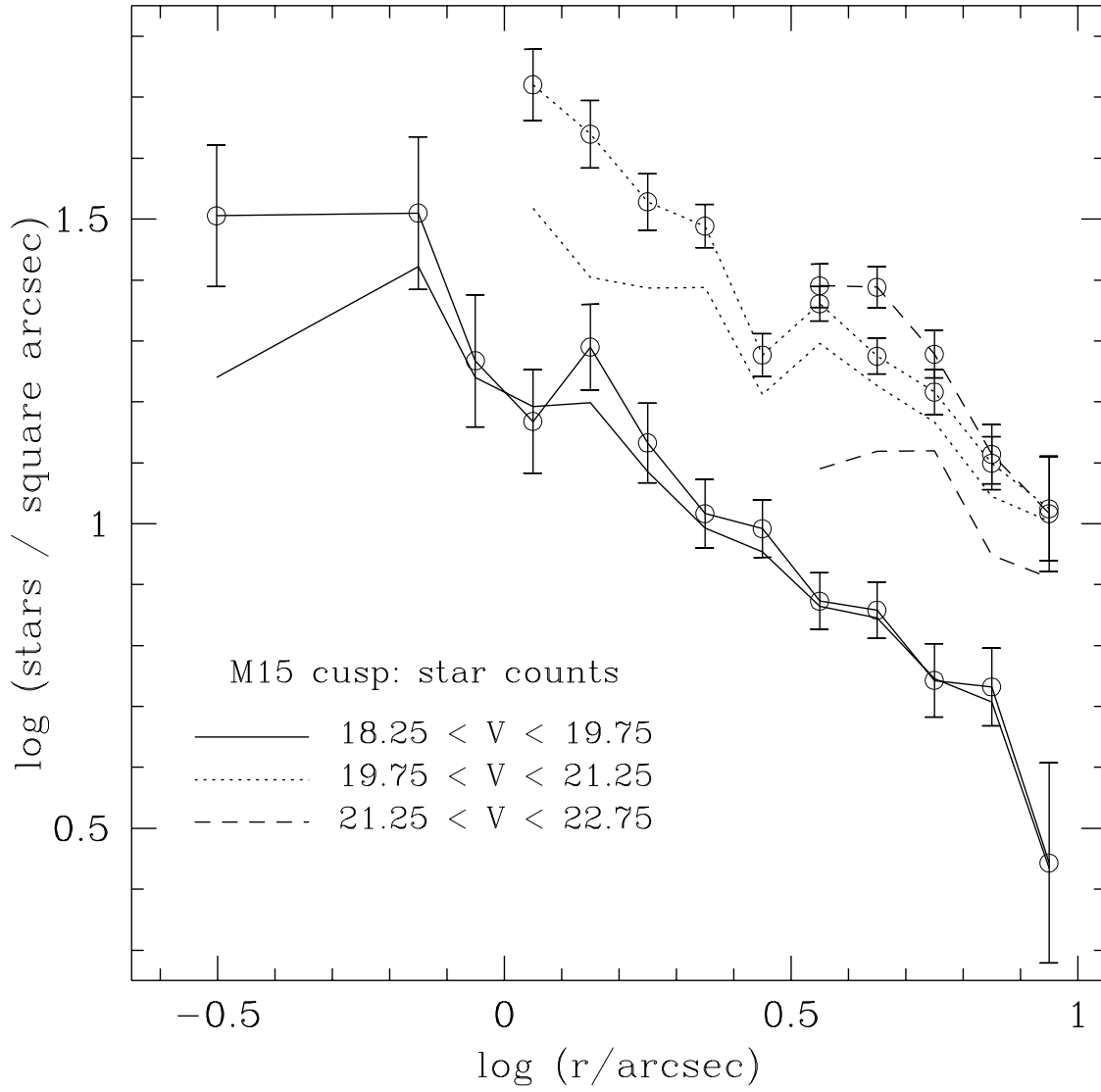


Figure 6

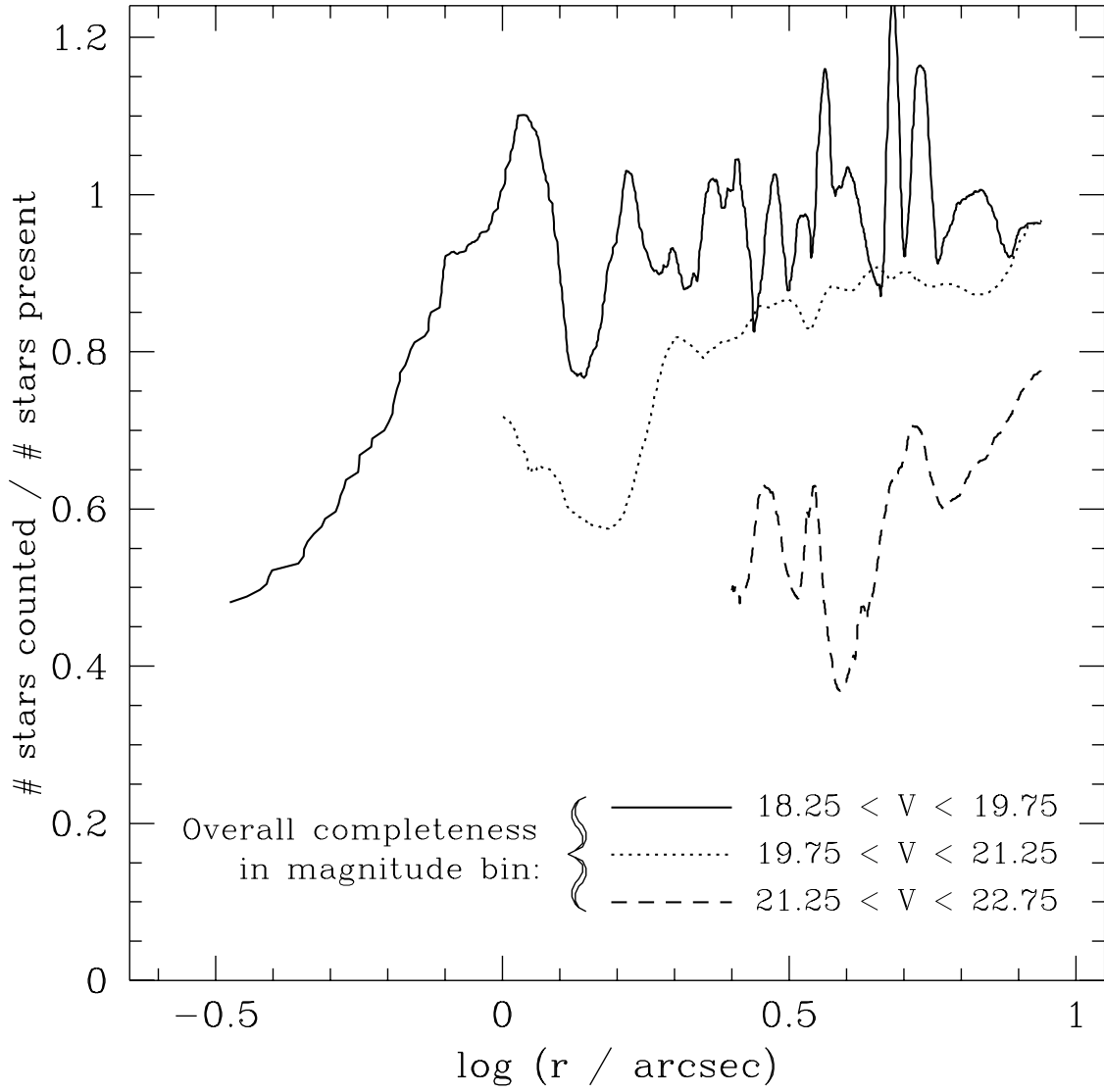


Figure 7

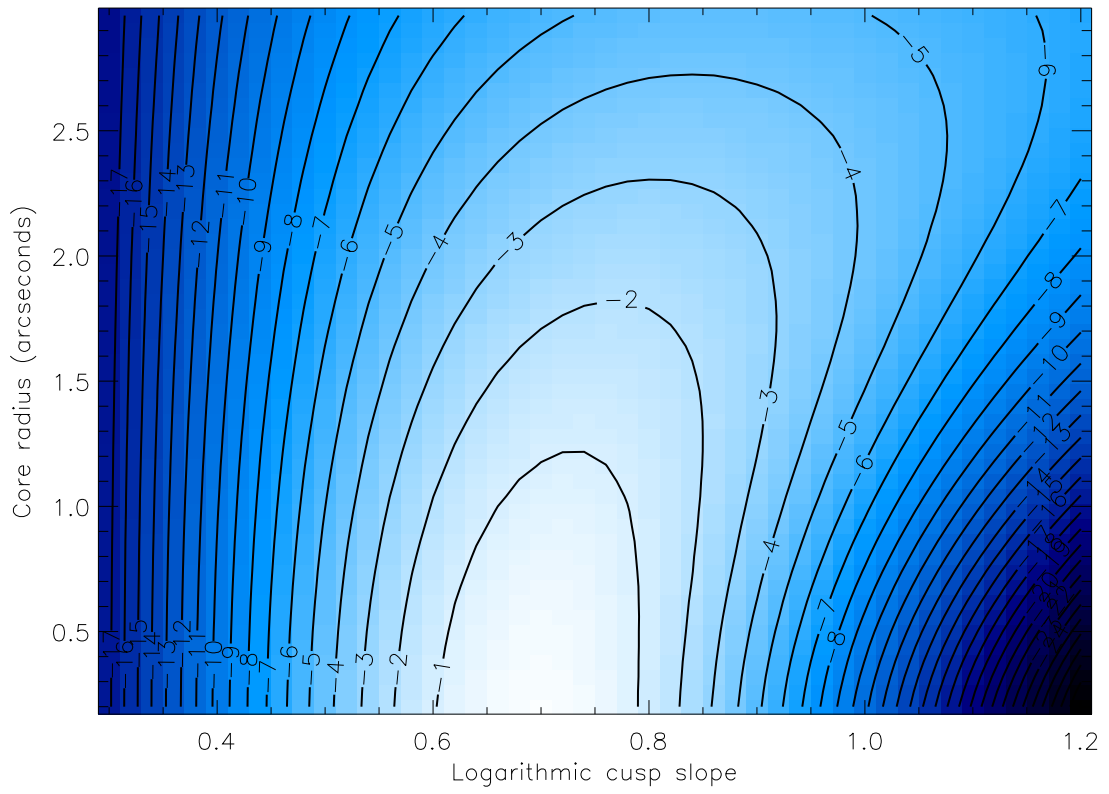


Figure 8

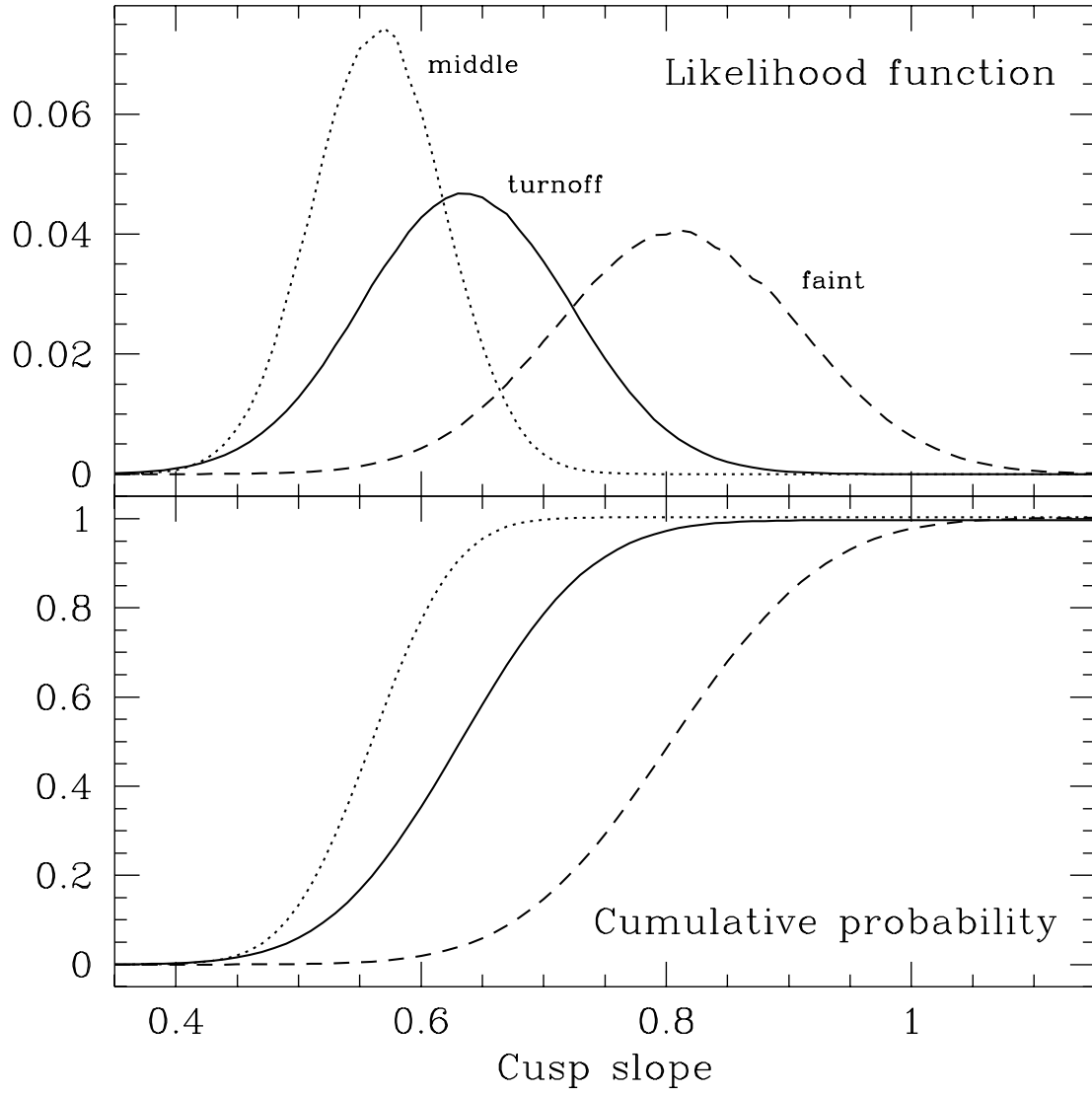


Figure 9

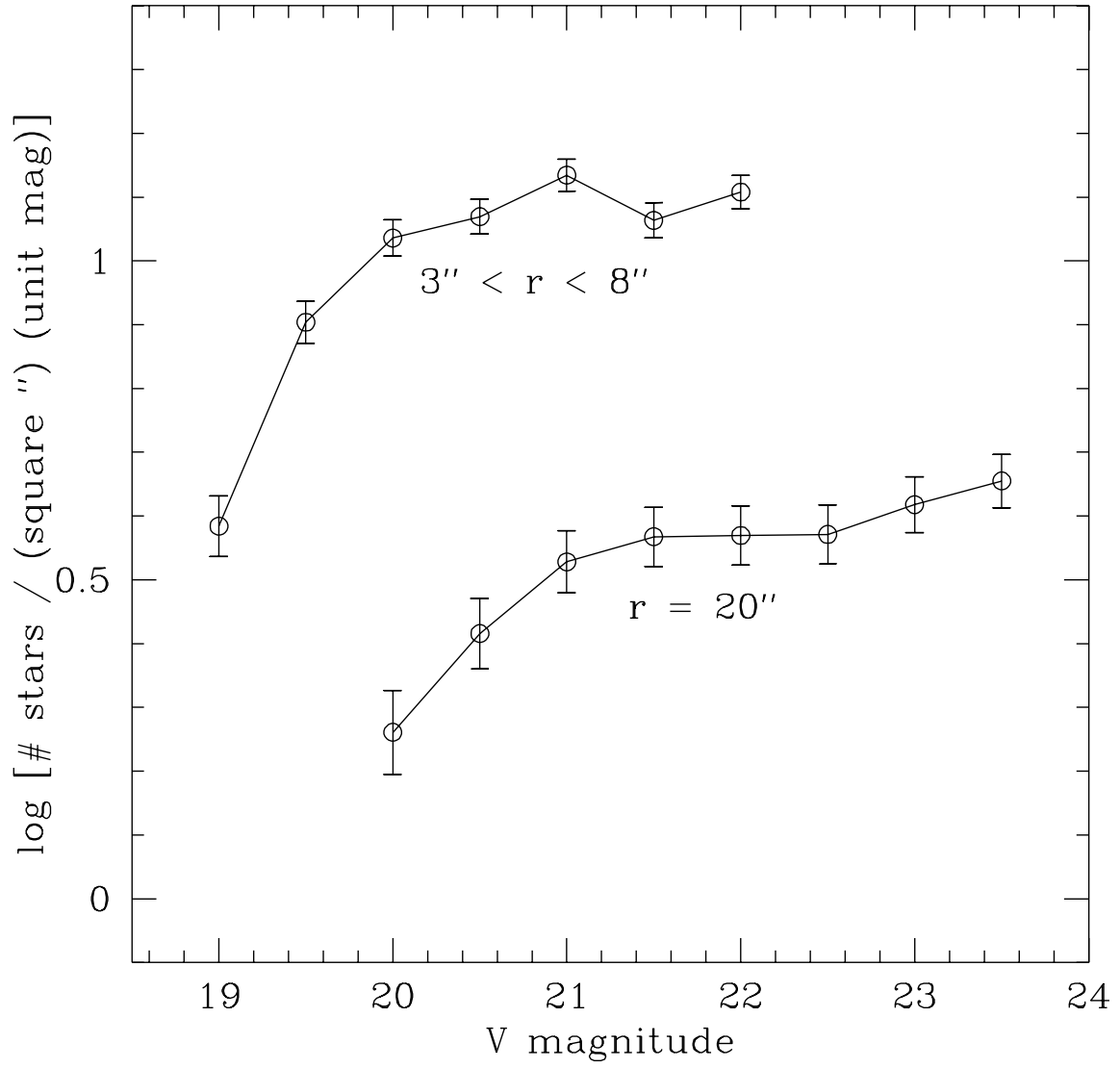


Figure 10

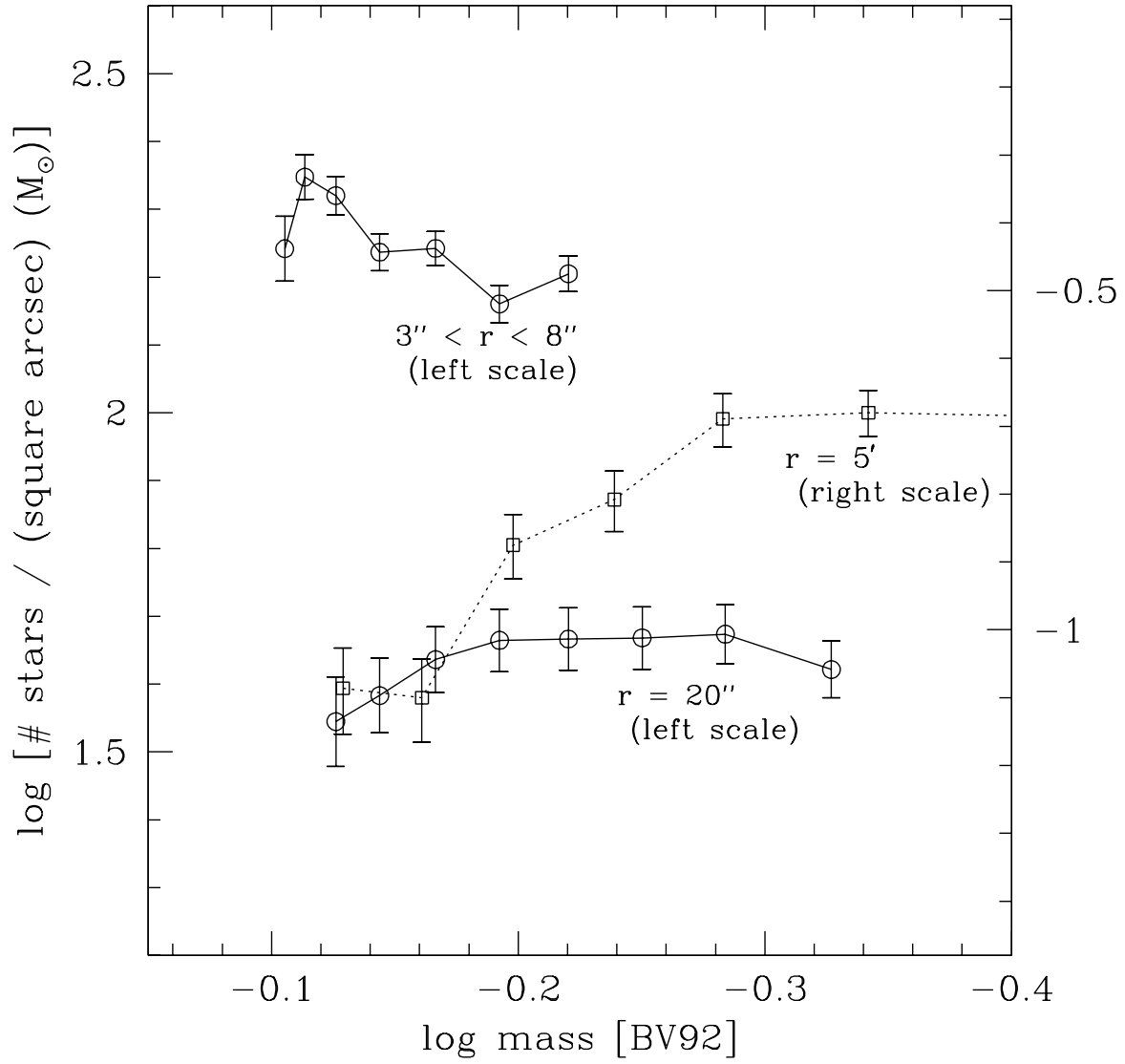


Figure 11

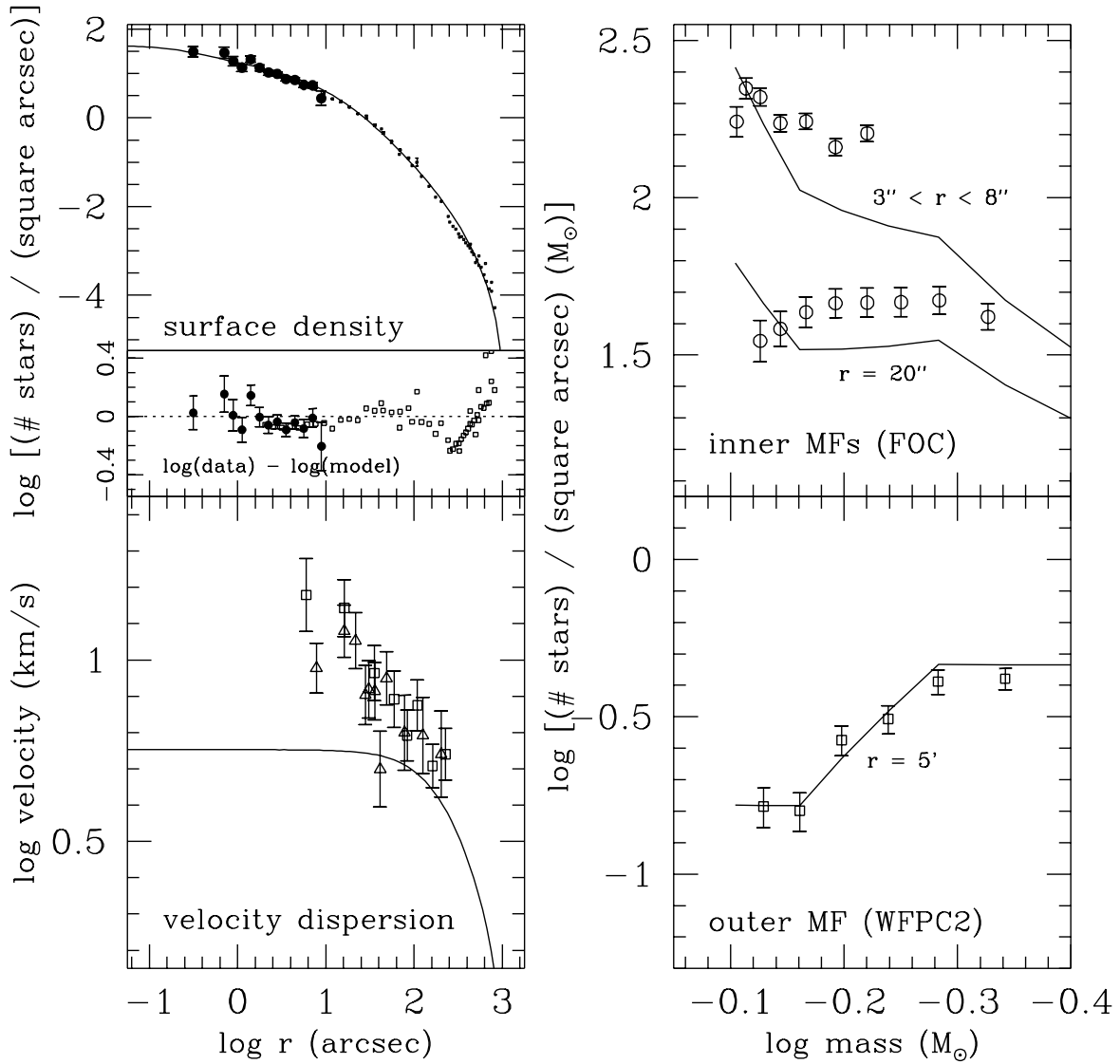


Figure 12